ACS Photonics

pubs.acs.org/journal/apchd5

Article

Goos−Hänchen Shift Spatially Resolves Magneto-Optical Kerr Effect Enhancement in Magnetoplasmonic Crystals

Anastasia V. Makarova, Anastasia A. Nerovnaya, Dmitry N. Gulkin, Vladimir V. Popov, Aleksandr Yu. Frolov, and Andrey A. Fedyanin*

Cite This: *ACS Photonics* 2024, 11, 1619−1626

ABSTRACT: We report on how observation of the Goos−Hänchen (GH) shift can be used to spatially resolve the transverse magneto-optical Kerr effect (TMOKE) enhancement in all-nickel magnetoplasmonic crystals (MPCs). First, the excitation of surface plasmons in the MPCs leads to a 15.3 μm (18λ) GH shift. Then, in the presence of a transverse magnetic field, the modulation of the lateral spatial intensity distribution of the reflected light [TMOKE(x)], caused by the GH shift, reaches 4.7% in the experiment. The spatially resolved TMOKE(x) values are several times higher compared to those from conventional TMOKE measurements in the MPCs. The concept of the spatially resolved magneto-optical effects under GH shift can be further extended to other magnetophotonic nanodevices for additional enhancing magneto-optical effects, sensing, and light modulation applications.

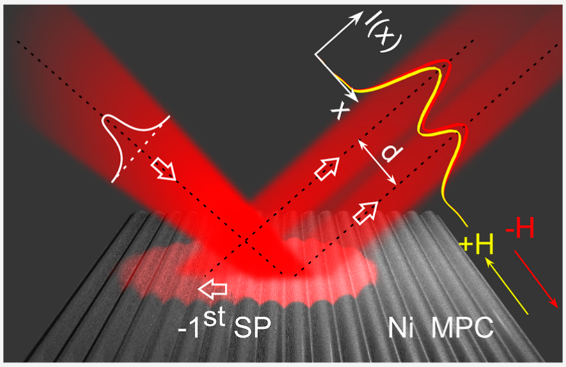

KEYWORDS: *Goos−Hänchen shift, magnetoplasmonics, magnetoplasmonic crystals, surface plasmons, transverse magneto-optical Kerr effect*

INTRODUCTION

The magneto-optical Kerr and Faraday effects play a key role in state-of-the-art nanophotonics. They allow the intensity, polarization, and phase of light to be controlled by an external magnetic field.[1] Since the values of magneto-optical effects are small for conventionally magnetically active materials,[2] their enhancement presents the main challenge in the modern magneto-optical research.[3−5] One of the ways to enhance the magneto-optical effects is to excite surface plasmons (SPs).[6] They represent collective oscillations of electromagnetic fields and conduction electrons propagating at the interface between a metal and a dielectric. The strong sensitivity of the SP to the dielectric permittivity at the metal/dielectric interface enables SP wavevector modulation in the presence of the magnetic field.[7−10] The magnetic field control of SP propagation becomes feasible by implementing magnetic materials in plasmonic crystals or thin metal films. Such magnetoplasmonic systems open up a range of approaches for controlling magneto-optical effects. In particular, the enhancement of the magneto-optical Kerr and Faraday effects has been observed in magnetoplasmonic crystals (MPCs)[11−16] which are periodically corrugated metal surfaces and one- or two-dimensional arrays of plasmonic nanoparticles. In order to additionally enhance the magneto-optical effects augmented by SP excitation, much research has been devoted to minimizing of absorption losses[17−19] and controlling the radiative losses of SPs.[20−22] Most works on the resonant enhancement of magneto-optical effects have not considered the spatial intensity distribution of reflected or transmitted beams. However, it is well known that the reflected light exhibits a lateral spatial shift, called the Goos−Hänchen (GH) shift (or the GH effect),[23] with respect to the direction predicted by geometrical optics. The strong SP field localization assists in the observation of the large GH shift. SP excitation in noble-metal-based plasmonic crystals enhances the GH shift up to several hundreds of wavelengths.[24,25] Moreover, the GH effect has been enhanced in different kinds of nanophotonic devices such as photonic crystals,[26,27] metamaterials,[28,29] and metasurfaces.[30] Since the discovery of the GH effect, it has found wide applications in SP-based sensors,[31,32] active optical switchers,[33,34] and optical differentiation devices.[35] Incorporating the magnetic materials into plasmonic and nonplasmonic platforms allows for the active control of the GH effect by an external magnetic field. The magnetic-field-induced modulation of the GH effect has been observed in nonplasmonic structures such as colloidal ferrofluid/air,[36] ferrite[37] interfaces, glass prism/magneto-optical waveguide structures,[38] magneto-

Received: December 14, 2023
Revised: February 29, 2024
Accepted: February 29, 2024
Published: March 18, 2024

https://doi.org/10.1021/acsphotonics.3c01844
ACS Photonics 2024, 11, 1619−1626

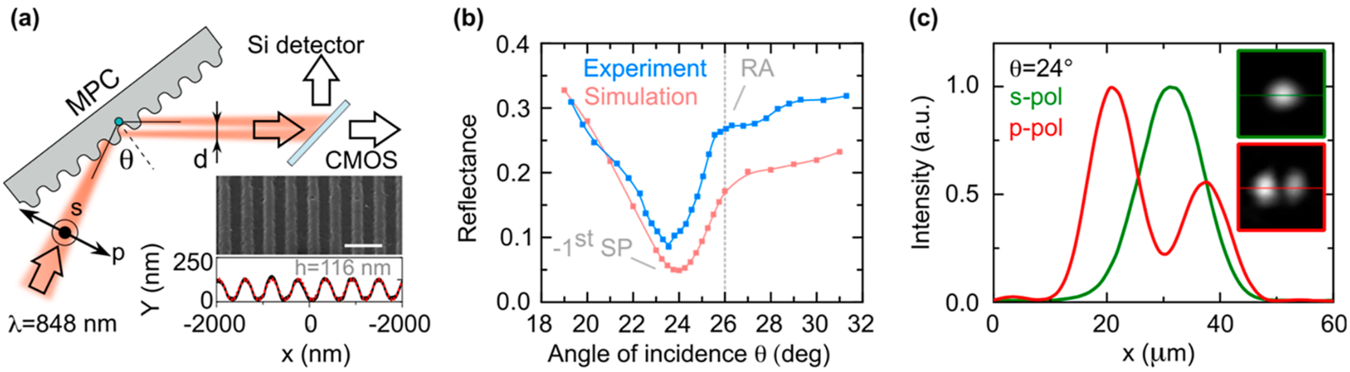

Figure 1. (a) Schematic of the experimental setup for measuring the angular dependence of reflectance and the GH effect. Inset: the SEM image (top) with a scale bar of 1 μm and the AFM cross section of the MPC (bottom). (b) Experimental (blue dots) and simulated (red dots) angular dependence of the MPC reflectance. (c) Intensity distribution of light on the MPC surface for $p-$ (red curve) and $s-$ (green curve) polarizations as the horizontal cross sections of the CMOS camera images shown in the inset. Incident angle is $\theta = 24°$.

photonic crystals in the GHz spectral range,[39] and in plasmonic thin films consisting of noble and ferromagnetic metals.[40]

In this work, we demonstrate how the GH effect in MPCs is capable of spatially resolving and ultimately benefiting the SP-assisted intensity modulation of light under an external magnetic field. First, the existence of the GH effect in one-dimensional all-nickel MPCs is shown. This effect is directly observed in the MPCs due to SP excitation. Then, by applying an external magnetic field to the MPCs in transverse geometry, we found that the spatial intensity distribution of the light beams is significantly modified under the GH effect. The observed lateral variation of the intensity [TMOKE(x)] is several times higher than that in the case of the conventional TMOKE measurements that reveal the total changes of the reflected beam intensity under a magnetic field.

■ EXPERIMENTAL METHODS

The MPC under analysis is represented as a one-dimensional nickel periodic grating with a quasi-sinusoidal surface profile (see the SEM image and the AFM cross section in Figure 1a).

The fit of the AFM cross section by harmonic function (red dots) reveals the corrugation depth of 116 ± 10 nm and a period of 575 nm. The detailed fabrication description can be found in Supporting Information SI1. Such a corrugation depth ensures the equality of radiative and absorption losses of the excited SPs in the MPC, leading to the highest values of electromagnetic field localization and the transverse magneto-optical Kerr effect (TMOKE).[21]

The measurements of the angular dependence of the reflectance and the GH effect were carried out by the experimental setup shown schematically in Figure 1a and detailed in Supporting Information SI2−SI4. Light from the collimated laser diode with a wavelength of $\lambda = 848 \pm 2$ nm passes through the liquid crystal retardation waveplates. The generated $p-$ or $s-$ polarized beam is focused onto the MPC surface. The focused beam has a beam waist of 10 μm approximated by the Gaussian beam function. The angular divergence of the beam is approximately 3°. The Si detector measures the intensity of the reflected beam, whereas the CMOS camera (ThorLabs DCC 1545 m) captures the spatial distribution of the reflected beam intensity.

■ RESULTS AND DISCUSSION

GH Effect in Ni MPC. The experimental angular dependence of the MPC reflectance is shown in Figure 1b. Rayleigh anomaly appears near $\theta = 26°$ and manifests itself as a small maximum. It is associated with the -1^{st} diffraction order when it propagates along the MPC surface. Reducing the incident angle fulfills the phase matching condition for excitation of the -1^{st} SP, which propagates in the negative direction. SP excitation results in a dip in the reflectance at $\theta = 24°$. The same minimum is present on the simulated angular reflectance dependence of the MPC (red curve and dots in Figure 1b), performed in the Lumerical FDTD commercial package.[41] The Gaussian beam with a beam waist of 10.3 μm, an angular divergence of 1.5°, and $\lambda = 848$ nm was used as a light source in the simulations. The modeled MPC surface consists of 125 periods and represents the harmonic function with a period of 590 nm and a corrugation depth of 117 nm. The monitor placed above the light source registers the MPC reflectance at a given angle of incidence.

To reveal the GH effect in the MPC under SP excitation, the spatial intensity distributions captured by the CMOS camera are shown in the insets in Figure 1c for $s-$ and $p-$ polarization. The angle of the incident light coincides with the reflectance dip ($\theta = 24°$) for $p-$ polarized light. For $s-$ polarization, the camera image has only a single spot associated with the mirror reflected beam. Under $p-$ polarization, the spatial distribution on the camera is modified compared with $s-$ polarization. The light intensity distribution on the MPC surface consists of two spots that manifest the GH effect in the nickel MPC under excitation of the -1^{st} SP.

The red and green curves in Figure 1c show the horizontal intensity cross section of the camera images along the beam centers obtained at $p-$ and $s-$ polarized incident light, respectively. The maxima of the two spots of the $p-$ polarized reflected beam are shifted in the positive and negative directions with respect to the single maximum of the specularly reflected $s-$ polarized beam. The appearance of the positively shifted beam is associated with a nonresonant mirror reflection of the incident light, while the negative shifted beam is associated with the -1^{st} SP excitation. The GH shift D is defined as the distance between the two maxima in the lateral direction of the reflected $p-$ polarized beam. It is obtained as $D = d \cos\theta$, where d is the distance between the two maxima measured on the camera. The GH shift is equal to $D = 15.3$ μm at the resonant angle of light incidence ($\theta = 24°$).

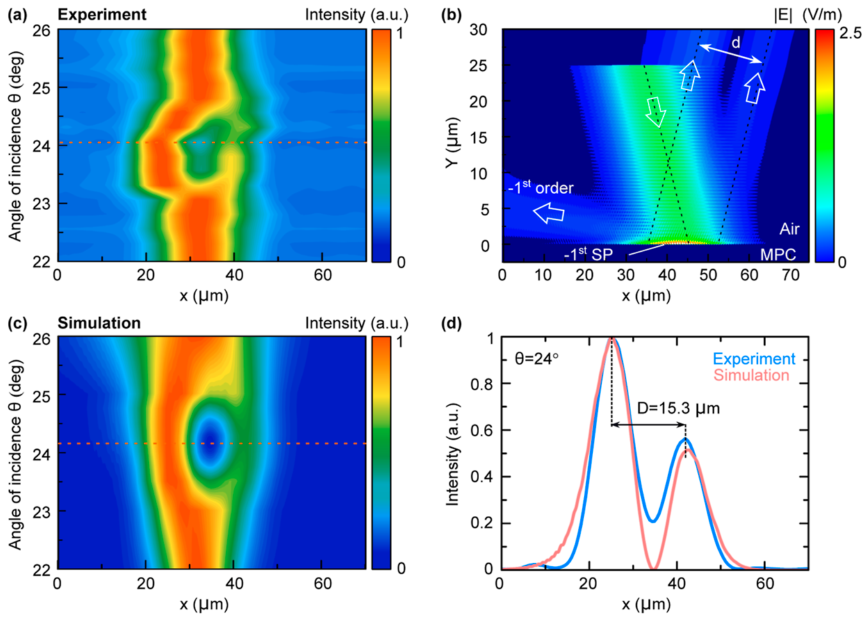

Figure 2. Angular dependence of the image cross section of the $p-$ polarized reflected beam, experimental (a) and simulated (c). (b) Simulation of the electric field distribution $|E(x, y)|$ under the GH effect in the MPC. (d) Experimental (blue curve) and simulated (red curve) cross sections of intensity profiles taken at the dashed lines marked on (a,c), respectively.

Angular Dependence of the GH Effect. The angular dependence of the GH effect and its dependence on SP excitation are demonstrated by the cross section of the camera images of the reflected $p-$ polarized beam. The experimental angular dependence is shown in Figure 2a in the range from $\theta = 22°$ to $\theta = 26°$. There is only one maximum on the dependence at off-resonant incident angles ($\theta > 25°$ and $\theta < 23°$), which means that the GH effect is no longer pronounced. However, one maximum is split into two near the SP resonant angle from $\theta = 23°$ to $\theta = 25°$. It manifests the GH effect enhanced by SP excitation. The maximum experimental GH effect is observed at $\theta = 24°$ and equal to $D = 15.3$ μm.

The GH effect in the MPC was also simulated in the Lumerical FDTD commercial package.[41] The parameters of the source and the MPC are the same as those in the angular reflectance dependence simulations. The monitor placed above the light source (12 μm from the MPC surface) registers the electric field distribution $|E(x)|$ along the x-axis. Figure 2b shows the electric field distribution $|E(x, y)|$ in the xy-plane at $\theta = 24°$. The incident light beam excites the -1^{st} SP by the -1^{st} diffraction order. The reflected beam is split into two, with the lateral distance D between them (distance along the x-axis), indicating the presence of the GH effect. One beam shifts in the negative direction due to the excitation of the-1^{st} SP, which propagates in the negative direction as well. The simulated angular dependence of $|E(x, y)|^2$ is shown in Figure 2c. The simulated results follow the same trend as the experimental ones. The GH effect is observed near the incident angle of $\theta = 24°$, corresponding to SP excitation. In the simulation, the maximum GH effect is $D = 15.9$ μm at $\theta = 24.2°$. SI4 in the Supporting Information shows that the change of the corrugation depth in the range from 90 to 125 nm preserves the GH shift value in the MPC. In contrast, the spatial distribution of the intensity $I(x)$ of the reflected beams is modified, and a good agreement with the experiment is only observed at $h = 117$ nm.

Combination of the Transverse Magneto-Optical Kerr and GH Effects. Figure 3a illustrates the idea of a magnetic-field-induced intensity modulation under the GH effect. Two static magnets with opposite directions are applied to the plane of the incident light in the transverse geometry, thus corresponding to the conventional measurements of TMOKE. In the conventional TMOKE, the intensity changes under an external magnetic field are integrated over the whole beam area, and such measurements are not sensitive to the spatial distribution of the reflected beam. In our experiment, the spatial cross section of the reflected beam intensity was recorded at each direction of the magnetic field $I(x, \pm H)$. The normalized difference of the intensity cross section $I(x, \pm H)$ under two opposite transverse magnetic field directions defines the spatially resolved TMOKE(x)

$$\mathrm{TMOKE}(x) = 2 \times \frac{I(x, +H) - I(x, -H)}{I(x, +H) + I(x, -H)} \times 100\% \quad (1)$$

Figure 3b,c demonstrates the experimental intensity cross sections of the reflected beam $I(x, \pm H)$ (black and red curves, respectively) recorded at the two opposite directions of the magnetic fields and TMOKE(x) (blue curves) measured at $\theta = 23.8°$ and $\theta = 24.3°$. These two incident angles correspond to the angular vicinity where the GH effect is at a maximum (Figure 2a). Moreover, they are on the decreasing and increasing sides of the angular reflectance dependence, respectively (Figure 1b). $I(x, H)$ and $I(x, -H)$ differ from each other. TMOKE(x) dependences (blue curves in Figure 3b,c) reflect the quantitative values of the difference between $I(x, +H)$ and $I(x, -H)$. The maximum TMOKE(x) values are reached at the minimum positions on the intensity cross sections $I(x, \pm H)$. The maximum TMOKE(x) values are 4.7% at $\theta = 23.8°$ and -4.0% at $\theta = 24.3°$. Figure 3d shows the full angular dependence of TMOKE(x) in the range of the incident angles from $\theta = 22°$ to $\theta = 26°$. TMOKE(x) decreases when the incident angle detunes from the resonant one. Its

https://doi.org/10.1021/acsphotonics.3c01844
ACS Photonics 2024, 11, 1619−1626

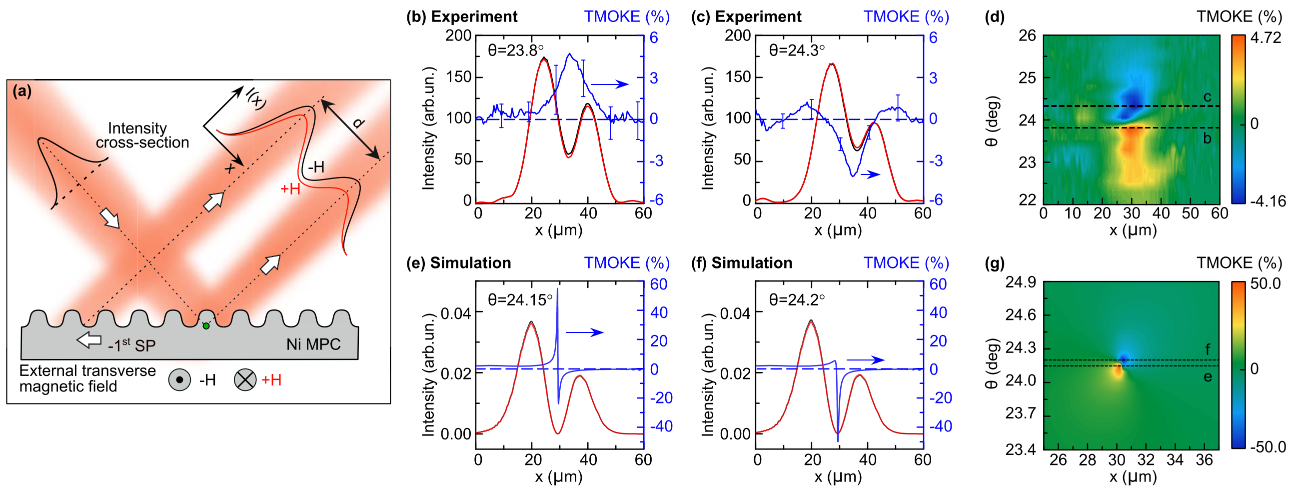

Figure 3. (a) Sketch of the spatial resolution of TMOKE observed under the GH effect in the MPC. Experimental (b,c) and simulated (e,f) intensity cross sections $I(x, \pm H)$ for various incident angles under an external transverse magnetic field applied to the MPC in opposite directions: black and red curves correspond to $I(x, +H)$ and $I(x, -H)$, respectively; blue curves are TMOKE(x) determined by eq 1. (d,g) Experimental and simulated angular dependence of TMOKE(x) in the MPC; spatial slices of the colormaps along the dashed lines marked as b,c,e,f are depicted in (b,c) and (e,f) graphs.

maximum spatial position on the incident angle is almost independent. Thus, the existence of the GH effect significantly modulates the TMOKE(x) spatial distribution.

The angular dependence of TMOKE(x) was simulated in the Lumerical FDTD package. The anisotropic tensor of Ni dielectric permittivity with nondiagonal components $\varepsilon_{xy} = ig$ and $\varepsilon_{yx} = -ig$, where g is Ni gyration constant, was introduced in the model meant to simulate the angular dependence of the GH effect. The Ni gyration constant $g = 0.062 - i0.3354$ at $\lambda = 848$ nm was taken from ref 2. TMOKE(x) reaches the maximum positive value of 54.9% at an incident angle of $\theta = 24.15°$ and $x = 29.2$ μm. This angle is located on the left side of reflectance minimum. For an incident angle of $\theta = 24.2°$, which coincides with the growing part of the reflectance angular dependence, TMOKE(x) changes the sign and reaches up to −50%.

The appearance of an inhomogeneous spatial distribution of TMOKE(x) emanates from a modification of the SP wavevector value under an external magnetic field in the transverse geometry. The magnetic field leads to a shift of the SP resonance angle in the MPC.[42−44] The change in the resonance angle also results in the angular shift of the GH effect angular dependence $I(x)$ shown in Figure 2a,c. Therefore, under the opposite directions of the magnetic field, the intensity cross sections $I(x, +H)$ and $I(x, -H)$ differ from each other.

The maximum TMOKE(x) values are achieved close to the minimum $I(x, \pm H)$ values, which emerged from the GH shift. Such enhancement of the intensity modulation in the vicinity of the minimum can be explained through the theory of the GH effect.[45] Under the GH effect in the MPC, the incident beam transfers its energy to the SP. SP propagates along the x axis and simultaneously radiates back into far-field in the direction of the specular reflected beam. There is a critical distance, x_c, at which the maximum intensity is carried by the SP field into the MPC. It is defined by the ratio, $w\alpha$, between beam waist w and propagation losses of an optical mode α. The SP propagation losses are high for the nickel MPC under study, providing $w\alpha \gg 1$ and $x_c \approx D/2$. A higher electromagnetic field localization near $x_c = D/2$ leads to greater magnetic-field-induced changes of the back-reflected light intensity. The difference between the maximum TMOKE(x) values in the experimental and simulated results is related to a mismatch in the angular beam divergence caused by the diffraction of the beam. The lower beam divergence used in the simulations results in a higher coupling efficiency of the incident Gaussian beam with SPs. It leads to a deeper minimum of $I(x)$ (see the difference of the dip on the red and blue $I(x)$ curves in Figure 2d) and therefore to a higher maximum TMOKE(x) value compared with the experimental result. The simulations in the Supporting Information (SI5) show that an increase in the Gaussian beam divergence up to 6° decreases the TMOKE(x) values compared to the similar ones observed in the experiment. However, the larger angular divergence of the beam leads to a mismatch of the spatial distribution of the intensity $I(x)$ in comparison with the experimental one. Moreover, Figure S5 in the Supporting Information (SI4) demonstrates that only a significant change of the corrugation depth from $h = 117$ nm reduces the spatially resolved TMOKE(x) values.

Comparison of the Spatially Resolved TMOKE(x) with the Conventional TMOKE. Finally, we compare the observed TMOKE(x) values with the conventional TMOKE measurements for the nickel MPC. TMOKE was measured as a normalized difference between the intensity of the reflected light $I(\pm H)$ taken at the opposite magnetic field directions in the transverse geometry

$$\mathrm{TMOKE} = 2 \times \frac{I(+H) - I(-H)}{I(+H) + I(-H)} \times 100\% \tag{2}$$

$I(\pm H)$ was measured by the silicon detector simultaneously with TMOKE(x) (more information on the measurements can be found in the Supporting Information, SI6). The experimental TMOKE angular dependence of Ni MPC is shown in Figure 4a as red dots. The TMOKE values possess sign change behavior near $\theta = 24°$ associated with the angular shift of the reflectance dependence under an external transverse magnetic field. Near this angle, TMOKE is higher than for other nonresonant angles. The maximum TMOKE value is 1.8%. Blue dots show the angular dependence of the

https://doi.org/10.1021/acsphotonics.3c01844
ACS Photonics 2024, 11, 1619−1626

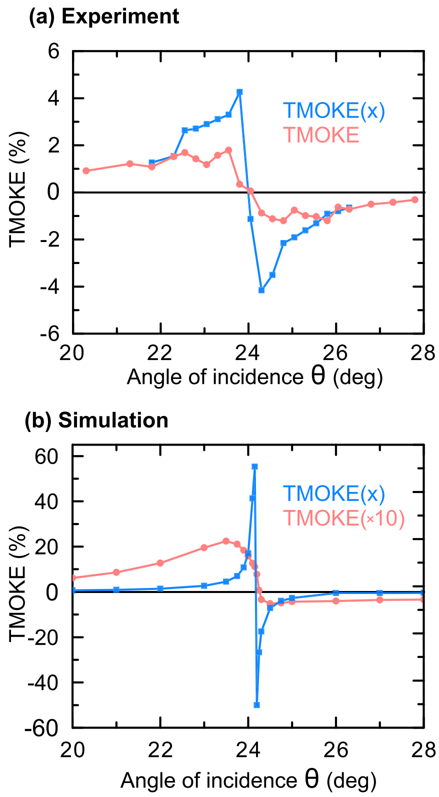

Figure 4. Experimental (a) and simulated (b) angular dependences of the TMOKE(x) maximum values (blue dots) and the conventional TMOKE (red dots).

maximum TMOKE(x) values (Figure 3c). TMOKE(x) has the same sign change trend as TMOKE. The observed maximum TMOKE(x) value of 4.7% exceeds the conventional TMOKE by 2.6 times (see Table 1). The comparison of the simulated angular dependence of TMOKE and the TMOKE(x) maximum values is shown in Figure 4b. TMOKE and TMOKE(x) also have sign changing behavior associated with the excitation of the −first SP. The maximum simulated TMOKE(x) value of 54.9% significantly exceeds the maximum TMOKE value of 2.2%, which qualitatively reproduces the experimental results. This increase arises from the spatial redistribution of SP energy near the MPC surface, which cannot be probed by the conventional TMOKE measurements. It should be noted that the angular dependence of TMOKE(x) is sharper than one of the conventional TMOKE. The found spatially resolved magneto-optical effects open up the direction to improve the sensitivity of magnetophotonic devices.

Table 1. Maximum TMOKE(x) and the Conventional TMOKE Values in the MPC

type	experiment, max %	simulation, max %
TMOKE(x)	4.7	54.9
TMOKE	1.8	2.2

■ CONCLUSIONS

To conclude, we show that the one-dimensional nickel MPC demonstrates the directly observed GH effect, which manifests itself in two reflected beams spatially separated by a distance D. The observed experimental shift between the mirror-reflected and shifted beams reaches up to $D = 15.3$ μm (18λ) and can be associated with surface plasmon excitation. In the external transverse magnetic field, the spatial distribution of intensity under the GH effect is noticeably modified at the position between the two reflected beams. The spatial resolution of TMOKE(x) leads to the maximum modulation intensity of 4.7% observed in the experiment. In comparison with the conventional TMOKE measurements, the maximum values of the spatially resolved TMOKE(x) are 2.6 times superior. Our findings can improve the functionality of magnetoplasmonic devices operating as sensors[46−53] and light modulators.[54−57] The spatially resolved magneto-optical effects associated with the GH shift can also be revealed in a wide range of nanophotonic devices such as magnetophotonic crystals,[58,59] plasmonic,[60,61] and low-loss all-dielectric metasurfaces.[62−66] Moreover, the observation of the GH shift can additionally boost the nonlinear magneto-optical,[67−71] ultrafast magneto-plasmonic,[72−74] and magnetoacoustic effects.[75,76]

■ ASSOCIATED CONTENT

Supporting Information

The Supporting Information is available free of charge at https://pubs.acs.org/doi/10.1021/acsphotonics.3c01844.

Sample characteristics and fabrication; AFM image of the MPC; experimental setup for angular measurements; detailed experimental scheme; angular dependence of the GH effect for $s-$ polarized incident light; camera image processing; influence of the corrugation depth of the Ni MPC on the GH shift and spatially resolved TMOKE(x); influence of the Gaussian beam angular divergence on the GH shift and spatially resolved TMOKE(x); and experimental setup for the TMOKE and the TMOKE(x) measurements (PDF)

■ AUTHOR INFORMATION

Corresponding Author

Andrey A. Fedyanin − *Faculty of Physics, Lomonosov Moscow State University, Moscow 199991, Russia;* orcid.org/0000-0003-4708-6895; Email: fedyanin@nanolab.phys.msu.ru

Authors

Anastasia V. Makarova − *Faculty of Physics, Lomonosov Moscow State University, Moscow 199991, Russia*

Anastasia A. Nerovnaya − *Faculty of Physics, Lomonosov Moscow State University, Moscow 199991, Russia*

Dmitry N. Gulkin − *Faculty of Physics, Lomonosov Moscow State University, Moscow 199991, Russia;* orcid.org/0000-0002-7694-7204

Vladimir V. Popov − *Faculty of Physics, Lomonosov Moscow State University, Moscow 199991, Russia*

Aleksandr Yu. Frolov − *Faculty of Physics, Lomonosov Moscow State University, Moscow 199991, Russia;* orcid.org/0000-0003-0988-1361

Complete contact information is available at: https://pubs.acs.org/10.1021/acsphotonics.3c01844

Notes

The authors declare no competing financial interest.

■ ACKNOWLEDGMENTS

The authors thank M.I. Sharipova, P.P. Kipp, A.A. Ezhov, and I.V. Soboleva for the experimental assistance. The experimental work was supported by the Russian Science Foundation, grant no. 20-12-00389. The numerical work was performed according to the Development Program of Lomonosov Moscow State University.

■ REFERENCES

(1) Zvezdin, A. K.; Kotov, V. A. *Modern Magnetooptics and Magnetooptical Materials*; CRC Press, 1997.

(2) Krinchik, G. S.; Artem'ev, V. A. Magneto-optical properties of Ni, Co, and Fe in the ultraviolet visible, and infrared parts of spectrum. *Sov. Phys. JETP* **1968**, *26*, 1080−1085.

(3) Kimel, A.; Zvezdin, A.; Sharma, S.; Shallcross, S.; de Sousa, N.; García-Martín, A.; Salvan, G.; Hamrle, J.; Stejskal, O.; McCord, J.; et al. The 2022 Magneto-Optics Roadmap. *J. Phys. D: Appl. Phys.* **2022**, *55*, 463003.

(4) Maccaferri, N.; Zubritskaya, I.; Razdolski, I.; Chioar, I.-A.; Belotelov, V.; Kapaklis, V.; Oppeneer, P. M.; Dmitriev, A. Nanoscale magnetophotonics. *J. Appl. Phys.* **2020**, *127*, 080903.

(5) Qin, J.; Xia, S.; Yang, W.; Wang, H.; Yan, W.; Yang, Y.; Wei, Z.; Liu, W.; Luo, Y.; Deng, L.; Bi, L. Nanophotonic devices based on magneto-optical materials: recent developments and applications. *Nanophotonics* **2022**, *11*, 2639−2659.

(6) Barnes, W. L.; Dereux, A.; Ebbesen, T. W. Surface plasmon subwavelength optics. *Nature* **2003**, *424*, 824−830.

(7) Armelles, G.; Cebollada, A.; García-Martín, A.; González, M. U. Magnetoplasmonics: Combining Magnetic and Plasmonic Functionalities. *Adv. Opt. Mater.* **2013**, *1*, 10−35.

(8) Singh, R. S.; Sarswat, P. K. From fundamentals to applications: The development of magnetoplasmonics for next-generation technologies. *Mater. Today Electronics* **2023**, *4*, 100033.

(9) Rizal, C.; Shimizu, H.; Mejía-Salazar, J. R. Magneto-Optics Effects: New Trends and Future Prospects for Technological Developments. *Magnetochemistry* **2022**, *8*, 94.

(10) Krinchik, G. S.; Chepurova, E. E.; Kraeva, T. I. Magneto-optical effects in nickel and permalloy associated with frustrated total internal reflection. *Sov. Phys. JETP* **1985**, *62*, 156−160.

(11) Kataja, M.; Hakala, T. K.; Julku, A.; Huttunen, M. J.; van Dijken, S.; Törmä, P. Surface lattice resonances and magneto-optical response in magnetic nanoparticle arrays. *Nat. Commun.* **2015**, *6*, 7072.

(12) Maccaferri, N.; Bergamini, L.; Pancaldi, M.; Schmidt, M. K.; Kataja, M.; Dijken, S. v.; Zabala, N.; Aizpurua, J.; Vavassori, P. Anisotropic Nanoantenna-Based Magnetoplasmonic Crystals for Highly Enhanced and Tunable Magneto-Optical Activity. *Nano Lett.* **2016**, *16*, 2533−2542.

(13) Grunin, A. A.; Zhdanov, A. G.; Ezhov, A. A.; Ganshina, E. A.; Fedyanin, A. A. Surface-plasmon-induced enhancement of magneto-optical Kerr effect in all-nickel subwavelength nanogratings. *Appl. Phys. Lett.* **2010**, *97*, 261908.

(14) Dyakov, S. A.; Fradkin, I. M.; Gippius, N. A.; Klompmaker, L.; Spitzer, F.; Yalcin, E.; Akimov, I. A.; Bayer, M.; Yavsin, D. A.; Pavlov, S. I.; Pevtsov, A. B.; Verbin, S. Y.; Tikhodeev, S. G. Wide-band enhancement of the transverse magneto-optical Kerr effect in magnetite-based plasmonic crystals. *Phys. Rev. B* **2019**, *100*, 214411.

(15) Kalish, A. N.; Komarov, R. S.; Kozhaev, M. A.; Achanta, V. G.; Dagesyan, S. A.; Shaposhnikov, A. N.; Prokopov, A. R.; Berzhansky, V. N.; Zvezdin, A. K.; Belotelov, V. I. Magnetoplasmonic quasicrystals: an approach for multiband magneto-optical response. *Optica* **2018**, *5*, 617−623.

(16) Khramova, A. E.; Ignatyeva, D. O.; Kozhaev, M. A.; Dagesyan, S. A.; Berzhansky, V. N.; Shaposhnikov, A. N.; Tomilin, S. V.; Belotelov, V. I. Resonances of the magneto-optical intensity effect mediated by interaction of different modes in a hybrid magnetoplasmonic heterostructure with gold nanoparticles. *Opt. Express* **2019**, *27*, 33170−33179.

(17) Temnov, V. V.; Armelles, G.; Woggon, U.; Guzatov, D.; Cebollada, A.; Garcia-Martin, A.; Garcia-Martin, J. M.; Thomay, T.; Leitenstorfer, A.; Bratschitsch, R. Active magneto-plasmonics in hybrid metal−ferromagnet structures. *Nat. Photonics* **2010**, *4*, 107−111.

(18) Chetvertukhin, A.; Musorin, A.; Dolgova, T.; Uchida, H.; Inoue, M.; Fedyanin, A. Transverse magneto-optical Kerr effect in 2D gold−garnet nanogratings. *J. Magn. Magn. Mater.* **2015**, *383*, 110−113.

(19) Pomozov, A. R.; Chekhov, A. L.; Rodionov, I. A.; Baburin, A. S.; Lotkov, E. S.; Temiryazeva, M. P.; Afanasyev, K. N.; Baryshev, A. V.; Murzina, T. V. Two-dimensional high-quality Ag/Py magneto-plasmonic crystals. *Appl. Phys. Lett.* **2020**, *116*, 013106.

(20) Frolov, A. Y.; Shcherbakov, M. R.; Fedyanin, A. A. Dark mode enhancing magneto-optical Kerr effect in multilayer magneto-plasmonic crystals. *Phys. Rev. B* **2020**, *101*, 045409.

(21) Kiryanov, M. A.; Frolov, A. Y.; Novikov, I. A.; Kipp, P. A.; Nurgalieva, P. K.; Popov, V. V.; Ezhov, A. A.; Dolgova, T. V.; Fedyanin, A. A. Surface profile-tailored magneto-optics in magneto-plasmonic crystals. *APL Photonics* **2022**, *7*, 026104.

(22) López-Ortega, A.; Zapata-Herrera, M.; Maccaferri, N.; Pancaldi, M.; Garcia, M.; Chuvilin, A.; Vavassori, P. Enhanced magnetic modulation of light polarization exploiting hybridization with multipolar dark plasmons in magnetoplasmonic nanocavities. *Light Sci. Appl.* **2020**, *9*, 49.

(23) Goos, F.; Lindberg-Hänchen, H. Neumessung des Strahlversetzungseffektes bei Totalreflexion. *Ann. Phys.* **1949**, *440*, 251−252.

(24) Bonnet, C.; Chauvat, D.; Emile, O.; Bretenaker, F.; Le Floch, A.; Dutriaux, L. Measurement of positive and negative Goos−Hänchen effects for metallic gratings near Wood anomalies. *Opt. Lett.* **2001**, *26*, 666−668.

(25) Petrov, N. I.; Danilov, V. A.; Popov, V. V.; Usievich, B. A. Large positive and negative Goos-Hänchen shifts near the surface plasmon resonance in subwavelength grating. *Opt. Express* **2020**, *28*, 7552−7564.

(26) Soboleva, I. V.; Moskalenko, V. V.; Fedyanin, A. A. Giant Goos-Hänchen Effect and Fano Resonance at Photonic Crystal Surfaces. *Phys. Rev. Lett.* **2012**, *108*, 123901.

(27) Moskalenko, V. V.; Soboleva, I. V.; Fedyanin, A. A. Surface wave-induced enhancement of the Goos-Hänchen effect in one-dimensional photonic crystals. *JETP Lett.* **2010**, *91*, 382−386.

(28) Shadrivov, I. V.; Zharov, A. A.; Kivshar, Y. S. Giant Goos-Hänchen effect at the reflection from left-handed metamaterials. *Appl. Phys. Lett.* **2003**, *83*, 2713−2715.

(29) Xu, Y.; Chan, C. T.; Chen, H. Goos-Hänchen effect in epsilon-near-zero metamaterials. *Sci. Rep.* **2015**, *5*, 8681.

(30) Zheng, Z.; Zhu, Y.; Duan, J.; Qin, M.; Wu, F.; Xiao, S. Enhancing Goos-Hänchen shift based on magnetic dipole quasi-bound states in the continuum in all-dielectric metasurfaces. *Opt. Express* **2021**, *29*, 29541−29549.

(31) Chen, C.-W.; Lin, W.-C.; Liao, L.-S.; Lin, Z.-H.; Chiang, H.-P.; Leung, P.-T.; Sijercic, E.; Tse, W.-S. Optical temperature sensing based on the Goos-Hänchen effect. *Appl. Opt.* **2007**, *46*, 5347−5351.

(32) Wang, Y.; Zeng, S.; Crunteanu, A.; Xie, Z.; Humbert, G.; Ma, L.; Wei, Y.; Brunel, A.; Bessette, B.; Orlianges, J.-C.; Lalloué, F.; Schmidt, O. G.; Yu, N.; Ho, H.-P. Targeted Sub-Attomole Cancer Biomarker Detection Based on Phase Singularity 2D Nanomaterial-Enhanced Plasmonic Biosensor. *Nanomicro Lett.* **2021**, *13*, 96.

(33) Sun, D. A proposal for digital electro-optic switches with free-carrier dispersion effect and Goos-Hänchen shift in silicon-on-insulator waveguide corner mirror. *J. Appl. Phys.* **2013**, *114*, 104502.

(34) Wan, Y.; Zheng, Z.; Kong, W.; Zhao, X.; Liu, J. Fiber-to-Fiber Optical Switching Based on Gigantic Bloch-Surface-Wave-Induced Goos−Hänchen Shifts. *IEEE Photon. J.* **2013**, *5*, 7200107.

(35) Xu, D.; He, S.; Zhou, J.; Chen, S.; Wen, S.; Luo, H. Goos−Hänchen effect enabled optical differential operation and image edge detection. *Appl. Phys. Lett.* **2020**, *116*, 211103.

(36) Fu, M.; Zhang, Y.; Wu, J.; Dai, X.; Xiang, Y. Large and negative Goos−Hänchen shift with magneto-controllability based on a ferrofluid. *J. Opt.* **2013**, *15*, 035103.
(37) Singh, I. J.; Nayyar, V. P. Lateral displacement of a light beam at a ferrite interface. *J. Appl. Phys.* **1991**, *69*, 7820−7824.
(38) Tang, T.; Qin, J.; Xie, J.; Deng, L.; Bi, L. Magneto-optical Goos-Hänchen effect in a prism-waveguide coupling structure. *Opt. Express* **2014**, *22*, 27042−27055.
(39) Ma, H.; Ju, C.; Xi, X.; Wu, R.-X. Nonreciprocal Goos-Hänchen shift by topological edge states of a magnetic photonic crystal. *Opt. Express* **2020**, *28*, 19916−19925.
(40) Tang, T.; Li, J.; Luo, L.; Shen, J.; Li, C.; Qin, J.; Bi, L.; Hou, J. Weak measurement of magneto-optical Goos-Hänchen effect. *Opt. Express* **2019**, *27*, 17638−17647.
(41) *Lumerical FDTD Solutions*, http://www.lumerical.com/ (accessed Febrary 2, 2022).
(42) Kushwaha, M. S.; Halevi, P. Magnetoplasmons in thin films in the Voigt configuration. *Phys. Rev. B* **1987**, *36*, 5960−5967.
(43) Chiu, K. W.; Quinn, J. J. Magnetoplasma Surface Waves in Metals. *Phys. Rev. B* **1972**, *5*, 4707−4709.
(44) Belotelov, V. I.; Bykov, D. A.; Doskolovich, L. L.; Kalish, A. N.; Zvezdin, A. K. Extraordinary transmission and giant magneto-optical transverse Kerr effect in plasmonic nanostructured films. *J. Opt. Soc. Am. B* **2009**, *26*, 1594−1598.
(45) Tamir, T.; Bertoni, H. L. Lateral Displacement of Optical Beams at Multilayered and Periodic Structures. *J. Opt. Soc. Am.* **1971**, *61*, 1397−1413.
(46) Grunin, A. A.; Mukha, I. R.; Chetvertukhin, A. V.; Fedyanin, A. A. Refractive index sensor based on magnetoplasmonic crystals. *J. Magn. Magn. Mater.* **2016**, *415*, 72−76.
(47) Maccaferri, N.; Gregorczyk, K. E.; de Oliveira, T. V. A. G.; Kataja, M.; van Dijken, S.; Pirzadeh, Z.; Dmitriev, A.; Åkerman, J.; Knez, M.; Vavassori, P. Ultrasensitive and label-free molecular-level detection enabled by light phase control in magnetoplasmonic nanoantennas. *Nat. Commun.* **2015**, *6*, 6150.
(48) Rizal, C.; Manera, M. G.; Ignatyeva, D. O.; Mejía-Salazar, J. R.; Rella, R.; Belotelov, V. I.; Pineider, F.; Maccaferri, N. Magnetophotonics for sensing and magnetometry toward industrial applications. *J. Appl. Phys.* **2021**, *130*, 230901.
(49) Murzin, D.; Mapps, D. J.; Levada, K.; Belyaev, V.; Omelyanchik, A.; Panina, L.; Rodionova, V. Ultrasensitive Magnetic Field Sensors for Biomedical Applications. *Sensors* **2020**, *20*, 1569.
(50) Belyaev, V. K.; Murzin, D. V.; Perova, N. N.; Grunin, A. A.; Fedyanin, A. A.; Rodionova, V. V. Permalloy-based magnetoplasmonic crystals for sensor applications. *J. Magn. Magn. Mater.* **2019**, *482*, 292−295.
(51) Knyazev, G. A.; Kapralov, P. O.; Gusev, N. A.; Kalish, A. N.; Vetoshko, P. M.; Dagesyan, S. A.; Shaposhnikov, A. N.; Prokopov, A. R.; Berzhansky, V. N.; Zvezdin, A. K.; Belotelov, V. I. Magnetoplasmonic Crystals for Highly Sensitive Magnetometry. *ACS Photonics* **2018**, *5*, 4951−4959.
(52) Belyaev, V. K.; Rodionova, V. V.; Grunin, A. A.; Inoue, M.; Fedyanin, A. A. Magnetic field sensor based on magnetoplasmonic crystal. *Sci. Rep.* **2020**, *10*, 7133.
(53) Kabashin, A. V.; Kravets, V. G.; Grigorenko, A. N. Label-free optical biosensing: going beyond the limits. *Chem. Soc. Rev.* **2023**, *52*, 6554−6585.
(54) Musorin, A. I.; Barsukova, M. G.; Shorokhov, A. S.; Luk'yanchuk, B. S.; Fedyanin, A. A. Manipulating the light intensity by magnetophotonic metasurfaces. *J. Magn. Magn. Mater.* **2018**, *459*, 165−170.
(55) Ignatyeva, D. O.; Krichevsky, D. M.; Belotelov, V. I.; Royer, F.; Dash, S.; Levy, M. All-dielectric magneto-photonic metasurfaces. *J. Appl. Phys.* **2022**, *132*, 100902.
(56) Damasceno, G. H. B.; Carvalho, W. O. F.; Cerqueira Sodré, A.; Oliveira, O. N. J.; Mejía-Salazar, J. R. Magnetoplasmonic Nanoantennas for On-Chip Reconfigurable Optical Wireless Communications. *ACS Appl. Mater. Interfaces* **2023**, *15*, 8617−8623.
(57) Carvalho, W. O. F.; Damasceno, G. H. B.; Moncada-Villa, E.; Mejía-Salazar, J. R. Active manipulation of radiated fields by a magnetoplasmonic half-wave dipole nanoantenna. *Opt. Lett.* **2023**, *48*, 680−683.
(58) Romodina, M. N.; Soboleva, I. V.; Musorin, A. I.; Nakamura, Y.; Inoue, M.; Fedyanin, A. A. Bloch-surface-wave-induced Fano resonance in magnetophotonic crystals. *Phys. Rev. B* **2017**, *96*, 081401.
(59) Romodina, M. N.; Soboleva, I. V.; Musorin, A. I.; Nakamura, Y.; Inoue, M.; Fedyanin, A. A. Bloch-surface-wave-induced Fano resonance in magnetophotonic crystals. *Phys. Rev. B* **2017**, *96*, 081401.
(60) Qin, J.; Deng, L.; Kang, T.; Nie, L.; Feng, H.; Wang, H.; Yang, R.; Liang, X.; Tang, T.; Shen, J.; Li, C.; Wang, H.; Luo, Y.; Armelles, G.; Bi, L. Switching the optical chirality in magnetoplasmonic metasurfaces using applied magnetic fields. *ACS Nano* **2020**, *14*, 2808−2816.
(61) Musorin, A. I.; Chetvertukhin, A. V.; Dolgova, T. V.; Uchida, H.; Inoue, M.; Luk'yanchuk, B. S.; Fedyanin, A. A. Tunable multimodal magnetoplasmonic metasurfaces. *Appl. Phys. Lett.* **2019**, *115*, 151102.
(62) Barsukova, M. G.; Shorokhov, A. S.; Musorin, A. I.; Neshev, D. N.; Kivshar, Y. S.; Fedyanin, A. A. Magneto-optical response enhanced by Mie resonances in nanoantennas. *ACS Photonics* **2017**, *4*, 2390−2395.
(63) Chernyak, A. M.; Barsukova, M. G.; Shorokhov, A. S.; Musorin, A. I.; Fedyanin, A. A. Bound States in the Continuum in Magnetophotonic Metasurfaces. *JETP Lett.* **2020**, *111*, 46−49.
(64) Ignatyeva, D. O.; Karki, D.; Voronov, A. A.; Kozhaev, M. A.; Krichevsky, D. M.; Chernov, A. I.; Levy, M.; Belotelov, V. I. All-dielectric magnetic metasurface for advanced light control in dual polarizations combined with high-Q resonances. *Nat. Commun.* **2020**, *11*, 5487.
(65) Zimnyakova, P. E.; Ignatyeva, D. O.; Karki, D.; Voronov, A. A.; Shaposhnikov, A. N.; Berzhansky, V. N.; Levy, M.; Belotelov, V. I. Two-dimensional array of iron-garnet nanocylinders supporting localized and lattice modes for the broadband boosted magneto-optics. *Nanophotonics* **2021**, *11*, 119−127.
(66) Bsawmaii, L.; Gamet, E.; Lefkir, Y.; Neveu, S.; Jamon, D.; Royer, F. Large reciprocal magneto-optical effect induced by all-dielectric resonant gratings based on a magnetic nanocomposite. *New J. Phys.* **2023**, *25*, 063021.
(67) Razdolski, I.; Makarov, D.; Schmidt, O. G.; Kirilyuk, A.; Rasing, T.; Temnov, V. V. Nonlinear surface magnetoplasmonics in Kretschmann multilayers. *ACS Photonics* **2016**, *3*, 179−183.
(68) Tran, N.-M.; Chioar, I.-A.; Stein, A.; Alekhin, A.; Juvé, V.; Vaudel, G.; Razdolski, I.; Kapaklis, V.; Temnov, V. Observation of the nonlinear Wood's anomaly on periodic arrays of nickel nanodimers. *Phys. Rev. B* **2018**, *98*, 245425.
(69) Temnov, V. V.; Razdolski, I.; Pezeril, T.; Makarov, D.; Seletskiy, D.; Melnikov, A.; Nelson, K. A. Towards the nonlinear acousto-magneto-plasmonics. *J. Opt.* **2016**, *18*, 093002.
(70) Krutyanskiy, V. L.; Chekhov, A. L.; Ketsko, V. A.; Stognij, A. I.; Murzina, T. V. Giant nonlinear magneto-optical response of magnetoplasmonic crystals. *Phys. Rev. B* **2015**, *91*, 121411.
(71) Novikov, V. B.; Romashkina, A. M.; Ezenkova, D. A.; Rodionov, I. A.; Afanasyev, K. N.; Baryshev, A. V.; Murzina, T. V. Surface plasmon driven enhancement of linear and nonlinear magneto-optical Kerr effects in bimetallic magnetoplasmonic crystals in conical diffraction. *Phys. Rev. B* **2022**, *105*, 155408.
(72) Novikov, I. A.; Kiryanov, M. A.; Nurgalieva, P. K.; Frolov, A. Y.; Popov, V. V.; Dolgova, T. V.; Fedyanin, A. A. Ultrafast Magneto-Optics in Nickel Magnetoplasmonic Crystals. *Nano Lett.* **2020**, *20*, 8615−8619.
(73) Novikov, I. A.; Kiryanov, M. A.; Frolov, A. Y.; Popov, V. V.; Dolgova, T. V.; Fedyanin, A. A. Spatially Inhomogeneous Ultrafast Demagnetization of a Nickel Magnetoplasmonic Crystal. *JETP Lett.* **2023**, *118*, 574−578.

https://doi.org/10.1021/acsphotonics.3c01844
ACS Photonics 2024, 11, 1619−1626

(74) Shcherbakov, M. R.; Vabishchevich, P. P.; Frolov, A. Y.; Dolgova, T. V.; Fedyanin, A. A. Femtosecond intrapulse evolution of the magneto-optic Kerr effect in magnetoplasmonic crystals. *Phys. Rev. B* **2014**, *90*, 201405.
(75) Vlasov, V. S.; Lomonosov, A. M.; Golov, A. V.; Kotov, L. N.; Besse, V.; Alekhin, A.; Kuzmin, D. A.; Bychkov, I. V.; Temnov, V. V. Magnetization switching in bistable nanomagnets by picosecond pulses of surface acoustic waves. *Phys. Rev. B* **2020**, *101*, 024425.
(76) Alekhin, A.; Lomonosov, A. M.; Leo, N.; Ludwig, M.; Vlasov, V. S.; Kotov, L.; Leitenstorfer, A.; Gaal, P.; Vavassori, P.; Temnov, V. Quantitative ultrafast magnetoacoustics at magnetic metasurfaces. *Nano Lett.* **2023**, *23*, 9295−9302.

https://doi.org/10.1021/acsphotonics.3c01844
ACS Photonics 2024, 11, 1619−1626